

A Robust Bayesian Approach to Function Registration in \mathbb{R}^1

J. Derek Tucker^{a,*}, Lyndsay Shand^a, Kenny Chowdhary^a

^a*Sandia National Laboratories, Albuquerque, NM 87185*

Abstract

Functional data registration is a necessary processing step for many applications. The observed data can be inherently noisy, often due to measurement error or natural process uncertainty, which most functional alignment methods cannot handle. A pair of functions can also have multiple optimal alignment solutions which is not addressed in current literature. In this paper, we present a flexible Bayesian approach to functional alignment which appropriately accounts for noise in the data without any pre-smoothing necessary. Additionally, by running parallel MCMC chains, our method can account for multiple optimal alignments via the multi-modal posterior distribution of the warping functions. To most efficiently sample the warping functions, our approach relies on the ∞ -HMC sampling algorithm described in Beskos et al. (2017), a modification of the standard Hamiltonian Monte Carlo to be well-defined on the infinite-dimensional Hilbert space. We apply this novel and flexible Bayesian alignment method to both simulated data and real data to show its efficiency to handle noisy functions and successfully account for multiple optimal alignments in the posterior, characterizing the uncertainty surrounding the warping functions.

Keywords: amplitude variability, Bayesian model, function alignment, functional data analysis, phase variability

1. Introduction

Functional registration or time-warping, refers to the process of aligning two or more functions or curves in time and is often a pre-processing step necessary for appropriately analyzing such functions. By registering functions before performing statistical analysis on such functions, we can account for arbitrary reparameterizations of functions which can lead to incorrect analyses of many functional data applications such as the well-known growth rate curve analysis. Function registration is heavily relied upon in image and shape registration where analysis results can vastly differ depending on whether the data has been properly registered or not. More details on the importance of functional data registration can be found in [Srivastava and Klassen \(2016\)](#); [Marron et al. \(2015\)](#), and [Ramsay and Silverman \(2005\)](#). Functional data registration is also referred to as phase-amplitude separation because the underlying goal of the procedure is to effectively distinguish phase (x -axis) from amplitude (y -axis) variation. For example, in tracking the migration paths of birds or hurricanes, functional data registration would allow one to isolate the statistical variation

*Corresponding author. Tel.: +1 505 284 8415

Email addresses: jdtuck@sandia.gov (J. Derek Tucker), lshand@sandia.gov (Lyndsay Shand), kchowdh@sandia.gov (Kenny Chowdhary)

in the paths from the statistical variation in the speed of traversing the paths. The registration of a pair of functions results in an optimal warping function which enables one function to be aligned to the other. The resulting aligned functions characterize the amplitude variability while the warping function captures the phase variability between the two functions.

Early approaches to functional data alignment fall short in four major ways. (1) They lack the ability to characterize the uncertainty of the optimal warping function. (2) They assume the observed functions are naturally smooth and lack measurement error. (3) They do not consider more than one optimal alignment between a pair of functions. And lastly, (4) most methods do not use a proper distance as the objective function for registration.

Traditional approaches to functional data alignment, which are demonstrated in [Srivastava et al. \(2011b\)](#); [Ramsay and Silverman \(2005\)](#); [Sangalli et al. \(2010\)](#), and [Kneip and Ramsay \(2008\)](#), are not flexible enough to characterize the uncertainty of the resulting optimal alignment solution. These approaches make the common assumption that the functions to be aligned are smooth and thus they break down when a function exhibits too much noise. These methods usually rely on a derivative which are extremely noisy when the original functions are noisy, presenting additional computational challenges.

Recently, Bayesian frameworks have been proposed that can characterize the uncertainty of the warping function solution ([Telesca and Inoue, 2008](#); [Kurtek, 2017](#); [Lu et al., 2017](#); [Cheng et al., 2016](#)). Uncertainty quantification of the warping function is naturally done in the Bayesian framework through posterior inference. The clear difference between these approaches is in how they specify a prior on the space of the warping function as it lives on a nonlinear infinite dimensional manifold. The more recent Bayesian approaches by [Cheng et al. \(2016\)](#); [Lu et al. \(2017\)](#), and [Kurtek \(2017\)](#) rely on the square root velocity function (SRVF) representation of the warping function space introduced by [Srivastava et al. \(2011a\)](#) and [Srivastava et al. \(2011b\)](#) to simplify the complicated geometry. We will also take advantage of this transformation and provide more details in Section 2.

Only the most recently proposed approach of [Matuk et al. \(2019\)](#) has addressed the need to account for observed measurement error. All previous approaches, Bayesian or otherwise, have assumed the observed functions to be aligned are naturally smooth. Although smoothness is a convenient assumption, it can be an invalid one in many practical applications. Lastly, no current approaches consider the challenging case of multiple optimal alignments between a pair of functions or briefly mention a possible solution without application.

In this paper, we propose a hierarchical Bayesian approach to the registration of a pair of noisy functions on \mathbb{R}^1 and demonstrate its advantages over previously proposed registration algorithms. We propose a new framework for functional alignment which relies on a proper distance metric, is robust to noise, capable of characterizing the uncertainty of the warping function and finally, can account for multiple optimal alignments. The novelty of our new framework is the following: First, our approach accounts for measurement error, a challenge which has only recently been addressed by [Matuk et al. \(2019\)](#). Second, we favor the geometric Hamiltonian Monte Carlo algorithm of [Beskos et al. \(2017\)](#) (∞ -HMC) to more efficiently sample the warping function over algorithms and appropriately account for the geometry of the target space. And third, we employ parallel MCMC chains to capture multi-modal posterior distributions of our warping functions to reflect the case when there are multiple optimal alignments.

This paper is organized in the following way. Section 2 reviews pairwise functional registration in \mathbb{R}^1 , the general challenges associated and introduces the square-root velocity function repre-

sentation and proper distance metric relied upon throughout this paper. Section 3 specifies our hierarchical Bayesian model for registering a pair of noisy functions on \mathbb{R}^1 including our MCMC algorithm and multi-chain approach to the challenge of multiple alignments. In Section 4, we evaluate the approach on simulated functional data as well as two real data sets: a SONAR dataset that is naturally noisy and iPhone-collected accelerometer data with multiple possible alignments. Finally, we discuss the impact of this approach, extensions to multiple pairwise alignments, nontrivial extensions to functions on more complex geometries, and future work in Section 5.

2. A review of function registration in \mathbb{R}^1

Following the notation of [Tucker et al. \(2013\)](#) and without loss of generality, let f be a real-valued and absolutely continuous function on domain $[0, 1]$. Note that in practice, f is observed as discrete and interpolation can be used to more easily perform the requisite calculations. Let \mathbb{F} denote the set of all such functions and Γ denote the set of boundary-preserving diffeomorphisms: $\Gamma = \{\gamma : [0, 1] \mapsto [0, 1] \mid \gamma(0) = 0, \gamma(1) = 1\}$ such that the mapping $[0, 1] \mapsto [0, 1]$ is bijective (invertible) and differentiable. From this point on, we will refer to Γ as the set of warping functions. Then, for any $f \in \mathbb{F}$ and any $\gamma \in \Gamma$, $f \circ \gamma$ denotes the time-warping of f by γ .

For simplicity, consider the pairwise alignment problem where we wish to align functions $f_1, f_2 \in \mathbb{F}$. A simplified registration problem can be formulated by finding a warping, γ^* that minimizes the cost of translating f_2 to f_1 , for some chosen cost function.

$$\gamma^* = \operatorname{argmin}_{\gamma} \|f_1 - f_2 \circ \gamma\|^*,$$

where $\|\cdot\|^*$ is our distance metric yet to be chosen.¹ There are a few main challenges that all alignment approaches face and handle differently. One challenge of function alignment, as pointed out by [Srivastava et al. \(2011b\)](#) and [Tucker et al. \(2013\)](#), is finding a cost function to do the alignment that is both symmetric, that is, aligning f_1 to f_2 is the same as aligning f_2 to f_1 , and positive-definite, so that the metric is always non-negative and zero if and only if f_1 and f_2 are the same function after alignment. A natural choice is the usual \mathbb{L}^2 norm, denoted by $\|\cdot\|^2$, but it does not satisfy the symmetry requirement. More precisely,

$$\operatorname{argmin}_{\gamma} \|f_1 \circ \gamma - f_2\|^2 \neq \operatorname{argmin}_{\gamma} \|f_1 - f_2 \circ \gamma\|^2.$$

Second, there can be the issue of degeneracy in which case γ^* is so distorted it can align functions which should not be aligned, giving a false impression that these functions are *close* in the \mathbb{L}^2 sense when indeed they are not. Lastly, the \mathbb{L}^2 norm is not invariant under warping. That is,

$$\|f_1 - f_2\|^2 \neq \|f_1 \circ \gamma - f_2 \circ \gamma\|^2.$$

This means that two functions which are similar in an \mathbb{L}^2 sense, could be vastly different under the same warping, and vice versa.

To overcome these three challenges, we follow [Tucker et al. \(2013\)](#), [Cheng et al. \(2016\)](#) and [Lu et al. \(2017\)](#) and take advantage of the square-root velocity function (SRVF) representation

¹Although we are proposing a more robust approach, we are introducing a simplified registration problem to motivate the use of a proper distance metric.

introduced by [Srivastava et al. \(2011a\)](#). A function $f \in \mathbb{F}$ can be represented as a SRVF via the mapping:

$$q : [0, 1] \mapsto \mathbb{R}, \quad q(f(t)) = \text{sign}(\dot{f}(t))\sqrt{|\dot{f}(t)|} \text{ for any } f \in \mathbb{F}.$$

There is an equivalency, up to a constant, between the SRVF of f and f itself and it is given by $f(t) = f(0) + \int_0^t q(f(s))|q(f(s))|ds$, where $|\cdot|$ is the absolute value. Moreover, the SRVF of $f \circ \gamma$ is $(q \circ \gamma)\sqrt{\dot{\gamma}}$. The SRVF transformation lends itself naturally to the Fisher-Rao (FR) metric. It can be shown that the FR distance between two functions is equivalent to the \mathbb{L}^2 distance between their respective SRVF transformations, i.e., $\|f_1 - f_2\|_{FR} = \|q(f_1) - q(f_2)\|^2$ (see [Srivastava et al. \(2011b\)](#)). More importantly, the FR metric is phase invariant under warping, i.e., $\|f_1 \circ \gamma - f_2 \circ \gamma\|_{FR} = \|f_1 - f_2\|_{FR}$ and [Srivastava et al. \(2011a\)](#) shows that the FR metric is symmetric under warping as well, i.e., $\|f_1 \circ \gamma - f_2\|_{FR} = \|f_1 - f_2 \circ \gamma\|_{FR}$.

Following this framework and without loss of generality, we will align the SRVF of f_2 to the SRVF of f_1 , and then map the aligned functions back to the original space \mathbb{F} . In other words, we seek to estimate the warping function that minimizes $\|q_1 - (q_2, \gamma)\|^2$, where $(q_2, \gamma) = (q_2 \circ \gamma)\sqrt{\dot{\gamma}}$ and $q_i \doteq q(f_i(t))$ for $i = 1, 2$.

Additional challenges in function alignment come when placing the problem in a Bayesian framework, namely selecting a prior distribution for $\gamma \in \Gamma$. Recall that Γ is the space of diffeomorphic function mappings from $[0, 1] \mapsto [0, 1]$. Both optimization and Bayesian inference over this space is difficult, in particular, because this space is nonlinear and infinite dimensional. For example, the sum or scalar product of functions in Γ is not necessarily still contained in Γ . To overcome this difficulty, we follow the approach of [Lu et al. \(2017\)](#) which transforms γ to its corresponding SRVF representation and exploits the Riemannian-geometric structure of this transformation, and ultimately allows us to utilize more traditional inference or optimization algorithms that rely on the linearity of the underlying search space.

To understand how this transformation works, it is helpful to think of the set of warping functions Γ as the space of univariate cumulative distribution functions for random variables on $[0, 1]$. Then, for each $\gamma \in \Gamma$ there is an associated density function. Now, let $\psi = \sqrt{\dot{\gamma}}$ be the corresponding SRVF of γ and $\Psi^+ = \{\psi : [0, 1] \mapsto \mathbb{R}^+ \mid \|\psi\|^2 = 1\}$ ([Bhattachayya, 1943](#)) be the space of square-root densities (SRD). The SRD space is the positive orthant of the unit sphere in the Hilbert space $\mathbb{L}^2([0, 1])$ denoted by $\Psi\{\psi : [0, 1] \mapsto \mathbb{R} \mid \|\psi\|^2 = 1\}$. While this space is still infinite and nonlinear, it is much more simply defined and since the SRVF is a bijective mapping and $\gamma(0) = 0$, we can reconstruct γ by the inverse mapping $q^{-1}(\psi)(t) = \int_0^t \psi^2(s)ds$. We can further simplify, and even linearize Ψ^+ by mapping from the top half of the unit sphere onto a tangent space at ψ defined as

$$T_\psi(\Psi) = \{g \in \mathbb{L}^2 \mid \int_0^1 g(s)\psi(s)ds = 0\}.$$

For simplicity, we typically take $\psi = 1$, i.e., the identity function. Geometric details on $T_1(\Psi)$ can be found in [Srivastava et al. \(2007\)](#) and [Kurtek et al. \(2012\)](#); [Tucker et al. \(2013\)](#). The exponential map and its inverse can be used to map between Ψ and $T_1(\Psi)$:

$$\begin{aligned} \exp_1 : T_1(\Psi) &\mapsto \Psi & \exp_1(g) &= \cos(\|g\|) + \sin(\|g\|)\frac{g}{\|g\|}, & g \in T_1(\Psi) \\ \exp_1^{-1} : \Psi &\mapsto T_1(\Psi) & \exp_1^{-1}(\psi) &= \frac{\theta}{\sin(\theta)}(\psi - \cos(\theta)), & \theta = d(1, \psi), \quad \psi \in \Psi \end{aligned}$$

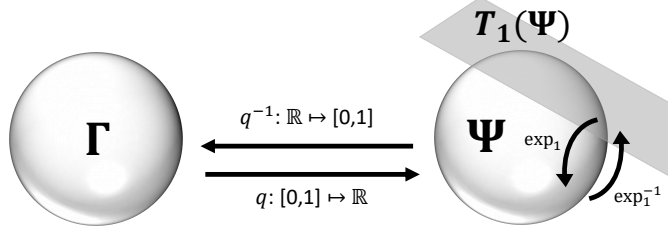


Figure 1: A summary of the mapping from Γ to $T_1(\Psi)$ where the space Γ is a nonlinear manifold and Ψ is the unit sphere in the Hilbert space $\mathbb{L}^2([0, 1])$

where $d(1, \psi) = \cos^{-1} \left(\int_0^1 \psi(t) dt \right)$. Mapping γ onto the tangent space $T_1(\Psi)$ (summarized in Figure 1) gives a convenient representation of γ in the parametric vector space and thus allows for a straight-forward prior specification to be placed on $T_1(\Psi)$ (discussed further in 3.1). Intuitively, this linearization is akin to mapping the points on the top half of the sphere to the tangent plane at the north pole. Moreover, because $T_1(\Psi)$ is the space of square integrable functions with mean zero, one can parameterize this space of functions with a basis representation.

Finally, through all of these transformations, the SRVF of $f_2 \circ \gamma$, denoted as $\mathcal{G}(g)$ can be written as

$$\begin{aligned} \mathcal{G}(g(t)) &:= (q_2, \gamma)(t) = q_2(\gamma(t)) \sqrt{|\dot{\gamma}(t)|} \\ &= q_2 \left(\int_0^t \psi^2(s) ds \right) \psi(t) = q_2 \left(\int_0^t \exp^2(g)(s) ds \right) \exp(g)(t). \end{aligned}$$

where g lives on the tangent space of Ψ^+ , which is again linear.

3. Pairwise registration in \mathbb{R}^1

First, we will detail our proposed approach in the simple case of pairwise alignment of functions y_1 and y_2 on \mathbb{R}^1 observed on a finite grid of lengths n_1 and n_2 respectfully. In this section, we will fully specify our proposed Bayesian hierarchical framework for this pairwise alignment setting.

Our Bayesian approach looks for optimal warping functions that warp one function to another using the \mathbb{L}^2 distance of the SRVF representations of the two functions as defined in the previous section. Furthermore, by mapping the space of warping functions to the linear tangent space $T_1(\Psi)$ on the infinite dimensional half sphere we can perform the Bayesian inference over a parametrized, linear space.

3.1. Model specification

Let y_1 and y_2 be noisy observations of $f_1, f_2 \in \mathbb{F}$, respectively. Then, at the first level of our hierarchical model we have,

Level 1.

$$y_1(t_i) = f_1(t_i) + \epsilon_1(t_i), \quad i = 1, \dots, n_1, \epsilon_1(t_i) \sim N(0, \sigma_1^2)$$

$$y_2(t_j) = f_2(t_j) + \epsilon_2(t_j), \quad j = 1, \dots, n_2, \quad \epsilon_2(t_j) \sim N(0, \sigma_2^2)$$

where the observed noise processes ϵ_1, ϵ_2 are assumed to follow a Gaussian white noise distribution with variances σ_1^2 and σ_2^2 , respectively, for each point in time. Here we assume no temporal correlation between noise parameters.

Using the SRVF representation described in Section 2, we aim to align $q_2(\gamma(t)) = q(f_2(\gamma(t)))$ to $q_1(t) = q(f_1(t))$. Using the transformations from the previous section, we can equate $q_2(\gamma(t))$ to $\mathcal{G}(g(t))$ where g is the projection of the square root density of γ onto the tangent space of the infinite half sphere and so we model $q_1(t) - \mathcal{G}(g(t))$ using a zero-mean multivariate Gaussian distribution following Lu et al. (2017). Thus, at the second level we have,

Level 2.

$$q_1(t) - \mathcal{G}(g(t)) \sim MVN(0_N, \sigma^2 I_{n_1})$$

with negative log-likelihood

$$\Phi(g) := -\log p(q_1, q_2; g) \propto \left(\frac{1}{\sigma^2}\right)^{n_1} \exp \left\{ -\frac{1}{2\sigma^2} \sum_{i=1}^{n_1} (q_1(t_i) - (q_2, \gamma)(t_i)) \right\}. \quad (3.1)$$

Following the approach of Lu et al. (2017), we will assign a zero-mean Gaussian process prior to the sampled tangent space $T_1(\Psi)$,

$$g \sim GP(0, \mathcal{C}).$$

with \mathcal{C} being a positive, self-adjoint and trace-class operator on \mathbb{R}^1 .

Zero-mean Gaussian process priors are assigned to mean functions f_1 and f_2 with structured kernel functions K_1 and K_2 :

$$f_1 \sim MVN(0, K_1), \quad f_2 \sim MVN(0, K_2).$$

In this work, we specify the squared exponential kernel function $K(\mathbf{t}) = s^2 \exp(-(d/2l)^2)$ for both K_1 and K_2 where d is the computed distance matrix of \mathbf{t} .

Conditionally-conjugate inverse-gamma priors are specified for all covariance parameters $\sigma^2, \sigma_1^2, \sigma_2^2$ with the prior for σ^2 should be less informative than prior for σ_1^2 and σ_2^2 to help with potential identifiability issues. Hyperparameters s_1^2, s_2^2 and l_1, l_2 are assigned inverse-gamma and uniform priors respectively.

The full hierarchical posterior can now be written as

$$p(g, \theta | y_1, y_2) = \left[\prod_{i=1}^2 p(y_i | f_i, \sigma_i^2) \right] \exp [-\Phi(g | f_1, f_2, \sigma^2)] \pi(g, \theta)$$

where $\theta \doteq \{f_1, f_2, \sigma^2, \sigma_1^2, \sigma_2^2, s_1^2, s_2^2, l_1, l_2\}$, $\pi(g, \theta)$ is the prior distribution over parameters g and θ , and $p(y_i | f_i, \sigma_i^2)$ for $i = 1, 2$ is a product of univariate Gaussian distributions.

3.2. MCMC sampling

A Metropolis within Gibbs sampler is used to sample from the complete posterior distribution $p(g, \theta | y_1, y_2)$. For practical implementation, functions f_1, f_2 are discretized and we specify a basis representation for g , i.e., $g = B\mathbf{v}$ where \mathbf{v} and B are the set of n_v basis coefficients and matrix of basis functions, respectively. The reason for this specification is as follows.

Recall that the g lives on $T_1(\Psi)$, the tangent space to the top half of the infinite-dimensional unit sphere at the point $\psi \in \Psi$. For simplicity, we take ψ to be the identity element so that T_1 becomes the space of all \mathbb{L}^2 integrable functions on $[0, 1]$ that have zero mean with respect to unit weight, i.e., the uniform density on the unit interval. Even though g is still infinite-dimensional, we can use a Fourier series type representation to parameterize g in terms of a finite collection of basis coefficients, \mathbf{v} , and discretized orthogonal basis vectors represented by columns of B . The choice of orthogonal basis functions are plentiful, but this paper uses Fourier series and Legendre polynomial expansions. Both sets form a complete basis over the space of \mathbb{L}^2 integrable functions on a compact interval. Moreover, for the application at hand, both basis functions (other than the constant) are orthogonal to the unit weight, thus making it easy to satisfy the tangent space property. The Fourier basis is typically used for periodic functions and so convergence can be hindered if the function values are different at the domain end points. Legendre polynomials do not have this limitation, but they are not as widely known. The smoother the function to be approximated is, the faster the decay of the basis coefficients, which means we need fewer basis coefficients to represent the underlying function. In fact, if the function is infinitely differentiable, the decay of the basis coefficients can be spectral, i.e., exponentially decaying. This applies to both Fourier and polynomial based expansions (see [Hesthaven et al. \(2007\)](#)). The basis specification for g thus allows us to more efficiently explore the posterior space $g|y_1, y_2, \theta$.

To update g , we wish to sample from the conditional posterior $p(g|y_1, y_2, \theta, B) \propto \exp(-\Phi(g))$. For efficient and robust sampling from $g|\cdot$, we will exploit Hamiltonian dynamics. Specifically we use the ∞ -HMC described in [Beskos et al. \(2017\)](#), a modification of the standard Hamiltonian Monte Carlo (HMC algorithm developed to be well-defined on the infinite-dimensional Hilbert Space. HMC is a natural choice for more complex geometries which allows for efficient sampling along posterior contours. As [Beskos et al. \(2017\)](#) describes, HMC is an improvement over the preconditioned Crank-Nicholson method, which itself is an improvement over the standard random walk Metropolis Hastings algorithm. Moreover, as we will show, in cases where the target density is multi-modal and separated by low probability regions, a parallel chain implementation with random starting points is needed to fully explore the state space (details given in Section 3.3) and for good exploration, it is required that we have highly efficient samplers for each parallel chain run.

The algorithm, detailed in Algorithm 1 utilizes an auxiliary variable. As suggested in [Beskos et al. \(2011\)](#) and implemented in [Beskos et al. \(2017\)](#), we choose to specify the auxiliary variable v , interpreted as the *velocity* of g . To implement Algorithm 1, to update g , it is necessary to define the location-specific preconditioner matrix $\mathcal{K}(g)$ as the covariance of a local Gaussian approximation $N(m(g), \mathcal{K}(g))$ to the posterior. We define this pre-conditioner through its inverse:

$$\mathcal{K}(g)^{-1} = \mathcal{C}^{-1} + \beta \mathcal{H}(g)$$

where $\mathcal{H}(g)$ is chosen as the Gauss-Newton Hessian (GNH), i.e.

$$\mathcal{H}(g) = \langle \nabla \mathcal{G}(g), \mathcal{C}^{-1} \nabla \mathcal{G}(g) \rangle.$$

We can then calculate the natural gradient η :

$$\eta(g) = -\mathcal{K}(g) [\nabla \Phi(g) - \beta \mathcal{H}(g)g]$$

to calculate the Hamiltonian flow, Ξ^t . As the exact analytic expression of Ξ^t is often not available, ∞ -HMC defines the flows Ξ_1^t, Ξ_2^t of a split Hamiltonian system to numerically approximate

$\Xi^t :$

$$\Xi_1^t(g, v) = \left(g, v + \frac{t}{2}\eta(g)\right) \text{ and } \Xi_2^t(g, v) = (g \cos t + v \sin t, -g \sin t + v \cos t)$$

The leapfrog map $\Psi_h(g, v) : (u_0, v_0) \mapsto (g_h, v_h)$ is the composition of three sub-steps:

$$\Psi_h(g, v) = \Xi_1^{h/2} \circ \Xi_2^h \circ \Xi_1^{h/2}$$

and the exact Hamiltonian flow Ξ^T is then approximated by

$$\Psi_h^I(g, v) = \Psi_h^{[T/h]},$$

a concatenation of $I = \lfloor T/h \rfloor$ Verlet steps. ∞ -HMC requires user chosen time-step h and leap-frog step T . $\nabla\Phi(g)$ is the directional derivative of Φ , defined in (3.1), with respect to g which is provided in the [Appendix A](#).

Compared to the *Z-mixture pCN algorithm* ([Cotter et al., 2013](#)) used in [Lu et al. \(2017\)](#) to update \mathbf{v} , we find that using ∞ -HMC algorithm to update g directly is significantly more efficient.

Algorithm 1 Sampling Algorithm for g via ∞ -HMC ([Beskos et al. \(2011\)](#))

1. Given current g , propose $g' = P_g\{\Psi_h^I(g, v)\}$ where $P_g\{\cdot\}$ is the projection of $(g', v') = \Psi_h^I(g, v)$ onto the g argument and v (velocity) is an auxiliary variable sampled from $N(0, \mathcal{C})$.
2. Accept g' with probability $1 \wedge \exp\{-\Delta H(g, v)\}$,

$$\Delta H(g, v) \equiv H(g', v') - H(g, v), \quad H(g, v) = \Phi(g) + \frac{1}{2}\langle g, \mathcal{C}^{-1}g \rangle + \frac{1}{2}\langle v, \mathcal{C}v \rangle.$$

Mean functions $f_1, f_2 \in \mathbb{R}^1$ are sampled from their respective conditional posteriors

$$p(f_k | y_k, \theta) \propto p(y_k | f_k, \sigma_k^2) p(q_k(t) - \mathcal{G}(g) | y_1, y_2, \theta) \pi(f_k), \quad k = 1, 2$$

via Metropolis-Hastings with specified proposals

$$f'_k(t_1), \dots, f'_k(t_{n_k}) \sim MVN(f_k(t_1), \dots, f_k(t_{n_k}), \Sigma_k^*), \quad k = 1, 2$$

and squared exponential correlation structures specified for Σ_1^* and Σ_2^* .

Variance parameters σ^2 , σ_1^2 , σ_2^2 and hyperparameters s_1^2 and s_2^2 can be Gibbs sampled from their respective inverse-gamma posteriors. Hyperparameters l_1 and l_2 can be sampled via Metropolis-Hastings with Gaussian proposal distributions and acceptance ratios:

$$\alpha_{l_k} = \frac{p(f_k | y_k, l'_k) \pi(l_k)}{p(f_k | y_k, l_k) \pi(l'_k)}, \quad k = 1, 2.$$

3.3. MCMC for multiple optimal alignments

Due to the high efficiency of the ∞ -HMC algorithm, a single posterior chain generated using ∞ -HMC would not be able to jump between modes and thus would be unable to capture multi-modal distributions. As highlighted by [Nishimura and Dunson \(2017\)](#), if the target distribution is multi-modal with modes separated by regions of low probability density, it is nearly impossible for any HMC algorithm to transition between modes due to the conservation of energy property of Hamiltonian dynamics. To obtain a multi-modal posterior distribution for $g|y_1, y_2, \theta$, we run K parallel chains with initial values for the basis coefficients of g chosen randomly from a standard Normal distribution.

The idea is to run separate chains at enough randomly generated starting points to land in the vicinity of the multiple modes so that we don't have to rely on the HMC algorithm to cross the low-probability regions. Of course, we have no idea where those modes are in general, so it is important to explore the initial starting space. In this case, the starting space is the space of coefficients, \mathbf{v} , of the linear expansion of g . Furthermore, under the assumption that each chain reaches their target sampling density after a thorough burn-in period, we can treat each chain as providing independent samples and thus simply pool them together. For example, if each of the ten chains produce 10k samples, we can pool them together to obtain 100k samples. Alternatively, we can think of this approach as a type of parallel MCMC with a constant temperature parameter and no mixing.

4. Examples

To demonstrate our proposed method, we will compare our flexible Bayesian approach with the state-of-the-art Dynamic Programming (DP) method of [Srivastava and Klassen \(2016\)](#). In short, the DP algorithm solves the optimal warping function by proposing successively better piecewise linear pathways on a unit square grid, where better is defined in terms of the Fisher-Rao metric.

First, we will assess our method's performance on simulated noisy data for which multiple optimal alignments exist. Next, we will apply our method to two real datasets: a SONAR dataset and an iPhone movement dataset. The SONAR data is notably noisy and thus difficult to register. The iPhone data is less noisy but has multiple optimal alignments that previous methods discussed in Section 1 do not account for.

Before we move on to the examples, we need to address the issue of computing means or averages in non-Euclidean geometries, e.g., the positive orthant of infinite-dimensional unit sphere. For problems of this type, we typically use the Karcher or Fréchet mean, which is obtained by minimizing the average squared distance between all pairs of sample points, $x_1, \dots, x_N \in \Psi$ i.e.

$$m = \arg \min_{p \in \Psi} \sum_{i=1}^N d^2(p, x_i),$$

where d is the metric or geodesic distance measure on Ψ , the infinite-dimensional positive orthant of the unit sphere, given by

$$d(\psi_1, \psi_2) = \cos^{-1} \left(\int_0^1 \psi_1(t) \psi_2(t) dt \right).$$

Note that in the case of Euclidean geometry, the Karcher mean is simply the average. The computation of the Karcher median is analogous. We use the method presented in [Xie et al. \(2017\)](#),

which is an extension of Algorithm 2 in [Tucker et al. \(2013\)](#). Now, in the multiple alignment case, our posterior will be multi-modal. In order to find the centroid of these individual modes, we do the following. We begin by computing all the pairwise distances under the metric d , between all posterior samples. We then use a clustering algorithm to separate the samples into their respective clusters. Then, for each cluster the Karcher mean or median can be computed as in the unimodal case.

4.1. Simulated data

Consider the misaligned and noisy observations y_1 and y_2 shown in Figure 2 simulated by adding Gaussian white noise with $\sigma_1^2 = \sigma_2^2 = 0.001$ to the true mean functions f_1 and f_2 . Without loss of generality, we wish to align y_2 to y_1 .

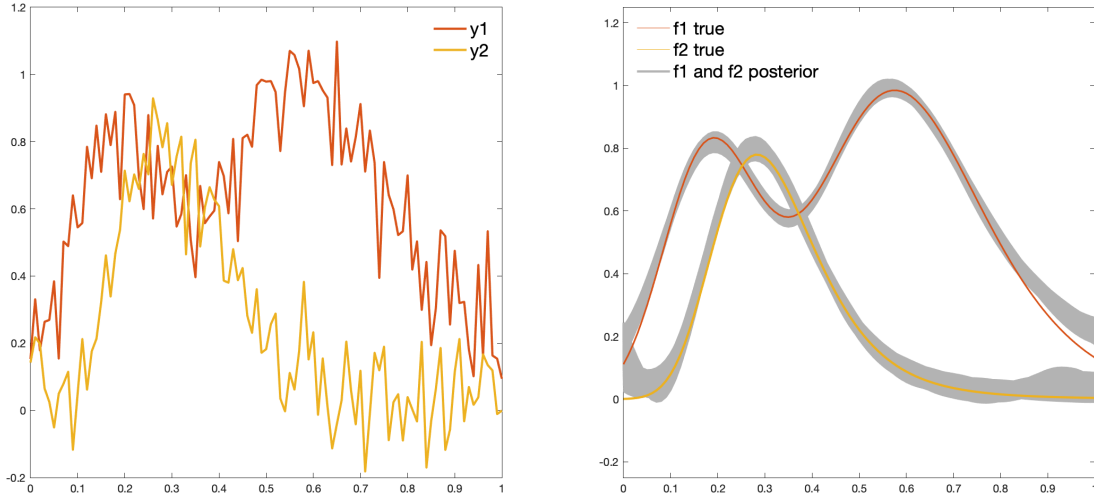


Figure 2: Simulations y_1 and y_2 (left) and their respective posteriors $f_1|y_1$ and $f_2|y_2$ (right) plotted against the true functions.

The right panel in Figure 2 shows the estimated posteriors for f_1 and f_2 given our Bayesian approach. Figure 3 compares the dynamic programming (DP) solution with our Bayesian approach. On the left, we see the optimal warping function for y_2 in blue, found by DP (γ_{DP}), which reflects some of the noise in the data and only identifies one possible warping function. The corresponding warped solution $y_2 \circ \gamma_{DP}$ is also shown in blue on the right. In our Bayesian approach, we ran 8 MCMC chains each with 20,000 iterations, a burn-in of 5,000 iterations without thinning, for a total of 4,000 effective samples. The proposal parameters were chosen such that acceptance rates for each chain were between 0.2 and 0.4 (see Figure B.9 for MCMC chains). Furthermore, we used $n_v = 10$ Fourier basis functions to approximate the function g on the tangent space $T_1(\Psi)$ resulting in a dimensionality of 20 (two for each basis function). The left figure of Figure 3 compares the posterior samples of $\gamma|y_1, y_2$ with credible intervals and posterior mode to the DP solution. The right figure of Figure 3 compares the posterior median warped solution to the DP warped solutions. From this we can see that the Bayesian approach gives us three possible solutions: (1) f_2 is aligned to the leftmost peak of f_1 , (2) f_2 is aligned to the rightmost peak of f_1 , and (3) f_2 is aligned to both peaks of f_1 . Note that the DP method only gives us one out of the possible three solutions.

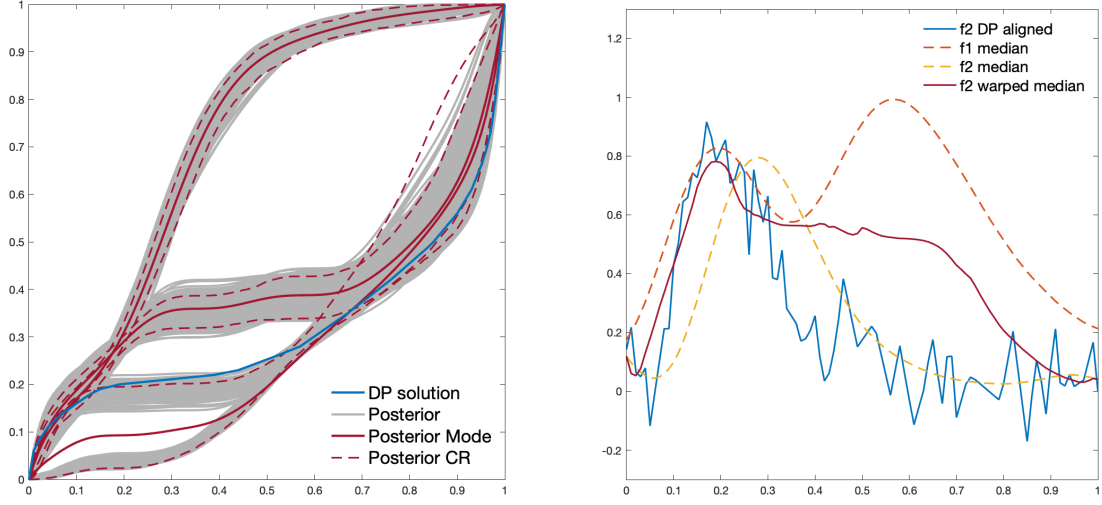


Figure 3: Comparison of the posterior distribution $\gamma|y_1, y_2$ to the DP solution γ_{DP} applied to the simulated data, plotting the two identified modes and respective 95% credible regions of the posterior $\gamma|y_1, y_2$ (left). Comparison of the DP warping of y_2 to the median of the warping $f_2 \circ \gamma|y_1, y_2$ (right).

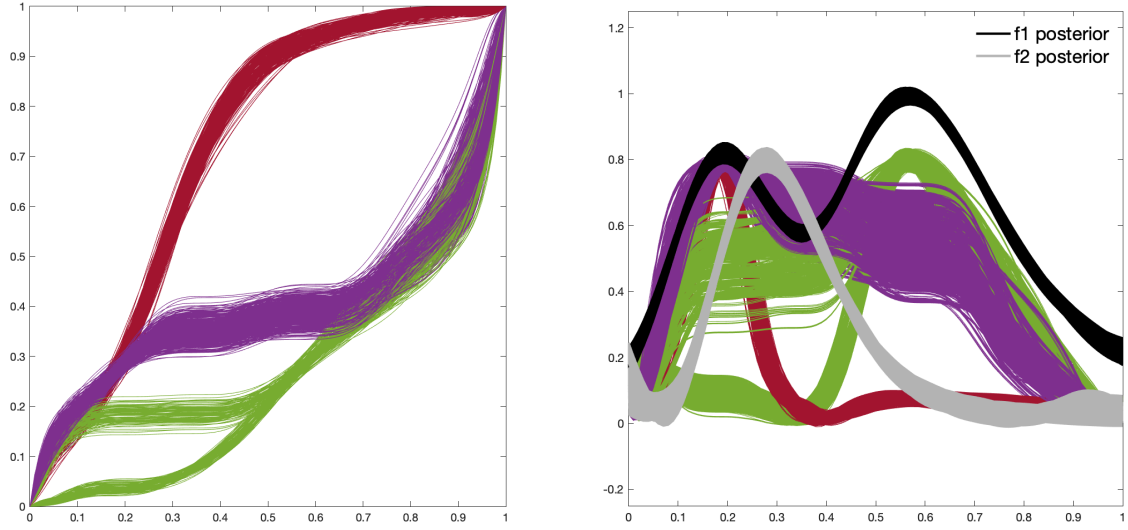


Figure 4: $\gamma|y_1, y_2$ (left) and $f_2 \circ \gamma|y_1, y_2$ (right) from the 8 different MCMC chains by color.

Further exploration of the Bayesian approach is shown in Figure 4. Here, we break down the posteriors $\gamma|y_1, y_2$ and $f_2 \circ \gamma|y_1, y_2$ from the 8 different MCMC chains by color. It is clear that 3 unique alignments were captured in the posteriors of $\gamma|y_1, y_2$ and $(f_2 \circ \gamma)|y_1, y_2$ among the 8 different MCMC chains, identified by three distinct colors. The left shows the three posterior modes and respective 95% credible regions, characterizing the uncertainty of each possible warping and the uncertainty of $(f_2 \circ \gamma)|y_1, y_2$, which is exhibited by the width of the color-coded samples on the right.

4.2. SONAR data

Next, we apply our alignment approach to naturally noisy SONAR data collected at the Naval Surface Warfare Center Panama City Division’s (NSWC PCD) test pond. For a description of the pond and measurement setup the reader is referred to [Kargl et al. \(2010\)](#). In short, the idea is to use the acoustic signals, generated from SONAR data, to discriminate and classify underwater “targets”, e.g., unexploded ordnance. More precisely, acoustic signals were generated from the raw SONAR data to construct “target strength” as a function of frequency and aspect angle. But due to the relatively small separation distances between the targets in the measurement setup, the scattered fields from the targets overlap leading to misaligned signatures, which could lead to erroneous identification and classification of the target. For this example, we took two such one-dimensional misaligned signatures, each with 1102 data samples, from a target that was a small, notched aluminum cylinder.

In our Bayesian approach, we ran 8 MCMC chains with 4,000 iterations each and a burn-in period of 2,000 steps without thinning, for a total of 16,000 samples. The proposal, prior, and hyperprior parameters were chosen such that acceptance rates were between 0.2 and 0.4 (see [Figure B.10](#) for MCMC chains). We additionally specified $n_v = 4$ Fourier basis functions to approximate g , as opposed to 8 in the previous example. We observed that reducing the number of basis functions n_v allowed our HMC algorithm to more easily explore the posterior space of g , likely by allowing the inference to focus entirely on the lower frequency basis elements. Lastly, due to the noisiness of this data, we only sampled 20% of the data, instead of the full set of 1102 data points, in order to obtain smooth estimates of f_1 and f_2 and avoid overfitting.

The posteriors $f_1|y_1$ and $f_2|y_2$ of the acoustic signatures from the SONAR data are shown in [Figure 5](#) on the left (gray) and right (in orange and yellow). On the right, we compare the DP aligned solution (in blue) and the Bayesian aligned solution (in gray). Note that our Bayesian approach offers multiple possible alignments, one of which is similar to the DP approach, but another which more accurately matches the maximum peaks of f_1 and f_2 .

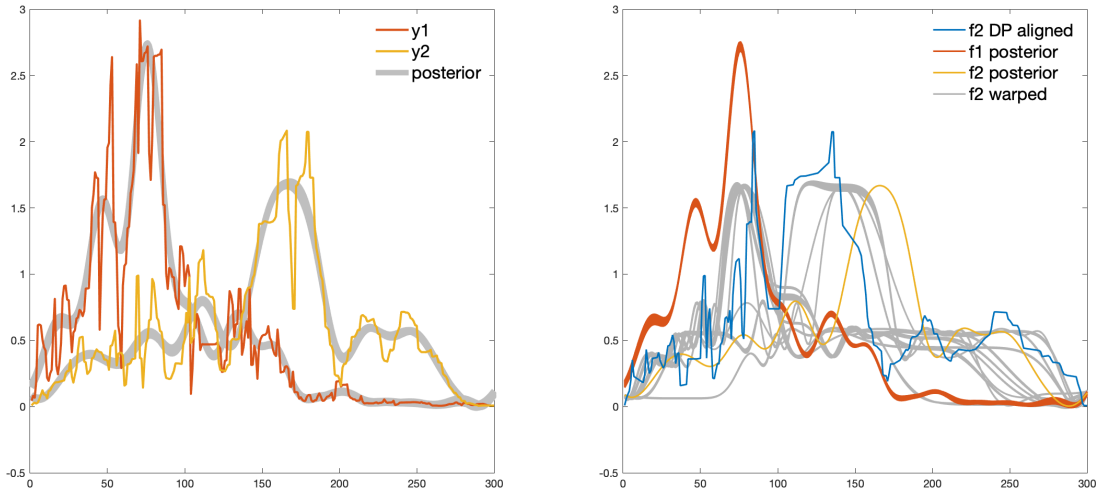


Figure 5: Posteriors $f_1|y_1$ and $f_2|y_2$ shown in gray compared to the raw data y_1 and y_2 (left). The posterior of the warped function $(f_2 \circ \gamma)|y_1, y_2$ captures more possible alignments than the single DP warped solution in blue (right).

Figure 6 on the right panel compares the MAP estimates to the DP solution. Figure 6 on the left compares the DP solution to the posterior distribution of $\gamma|y_1, y_2$ and shows the posterior

median and 95% credible region of $\gamma|y_1, y_2$. The credible region quantifies the uncertainty around the estimated warping function γ and thus the warped function $(f_2 \circ \gamma)$. Note that the credible region obtained from the Bayesian approach encapsulates the DP solution, which itself is not able to adequately account for the noise in the data. Subsequently, the uncertainty can be pushed through any later analyses for any quantity of interest that may depend on the aligned or warped functions. For example, any statistical moment calculations performed on the aligned functions, e.g., principal component analysis, can be modified to account for the uncertainty in the warping functions.²

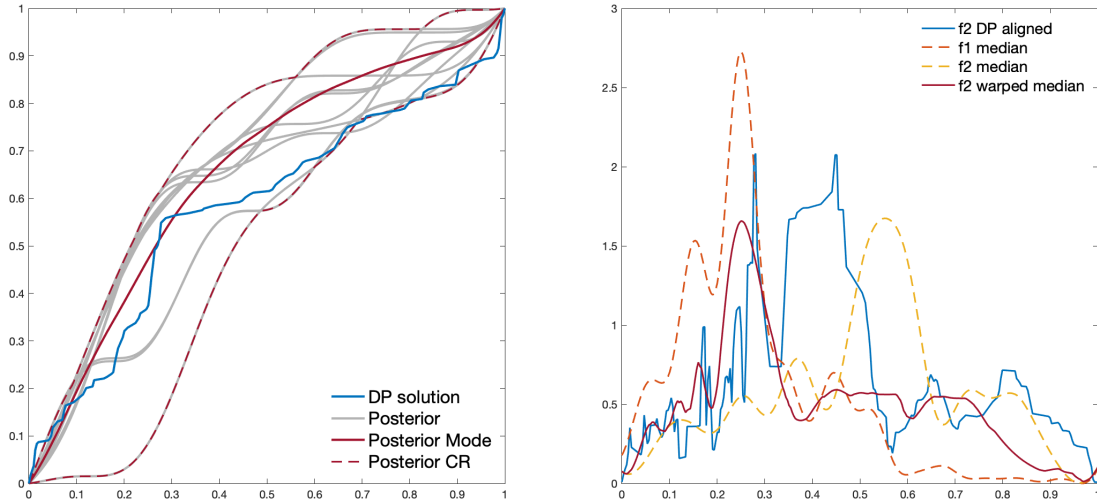


Figure 6: Comparison of the posterior distribution $\gamma|y_1, y_2$ to the DP solution γ_{DP} applied to the SONAR data, plotting the two identified modes and respective 95% credible regions of the posterior $\gamma|y_1, y_2$ (left). Comparison of the DP warping of y_2 to the median of the warping $f_2 \circ \gamma|y_1, y_2$ (right).

4.3. iPhone data

This data set consists of aerobic actions of subjects, such as biking, running, walking, etc., recorded using the Inertial Measurement Unit (IMU) on an Apple iPhone 4 smartphone, which these days is like using a cassette tape to listen to music. The IMU included a 3D accelerometer, gyroscope, and magnetometer. Each sample was taken at 60Hz, and manually trimmed to 500 samples (every 8.33s) to eliminate starting and stopping movements. For more information on the data set the reader is referred to [McCall et al. \(2012\)](#).

We chose to demonstrate our method on two of forty-five functional samples from the walking accelerometer data in the x -direction. In this context, we are specifically interested in the information contained in the separated phase and amplitude components rather than the resulting alignment. Consider, for example, we are only interested in the amplitude variability of the acceleration in the x -direction. Comparing the functions after warping would allow us to consider this variability. The two examples we are aligning, shown in the right figure of Figure 7, clearly have multiple possible alignments of y_2 to y_1 that we would like to also capture in the posterior $\gamma|y_1, y_2$.

To perform the Bayesian inference, we again ran 8 MCMC chains with 5,000 iterations each, a burn-in period of 1,000 steps, and thinning every other sample, for a total of 16,000 effective

²The most straightforward way to do this would be in Monte Carlo type fashion - compute the statistics for your quantity of interest (QoI) for each posterior sample $\gamma|y_1, y_2$, resulting in a histogram for the desired QoI.

samples. The proposal, prior and hyperprior parameters were chosen such that acceptance rates were between 0.2 and 0.4 (see Figure B.11 for MCMC chains). We additionally specified $n_v = 8$ Legendre basis functions to approximate g . We specify Legendre polynomials here since the data is non-periodic in nature.

The posteriors $f_1|y_1$ and $f_2|y_2$ can be seen in the left panel of Figure 7 along with y_1 and y_2 and the medians are shown in the right panel of Figure 8. This image also compares the DP aligned solution ($y_2 \circ \gamma_{DP}$) to the posterior alignment of $f_2|y_2$, $(f_2 \circ \gamma)|y_1, y_2$, from our Bayesian approach. It is clear that our Bayesian approach can capture multiple possible alignments, including alignments similar to the DP solution. For example, in addition to the alignment captured by the DP algorithm, the Bayesian approach also accounted for an alignment of f_2 to the leftmost peak of f_1 . It is interesting to note here that the method didn't match f_2 to the rightmost peak of f_1 . This would be caused by an extremely distorted warping function and the Fisher Rao metric natively guards against that by penalizing too high of a gradient.

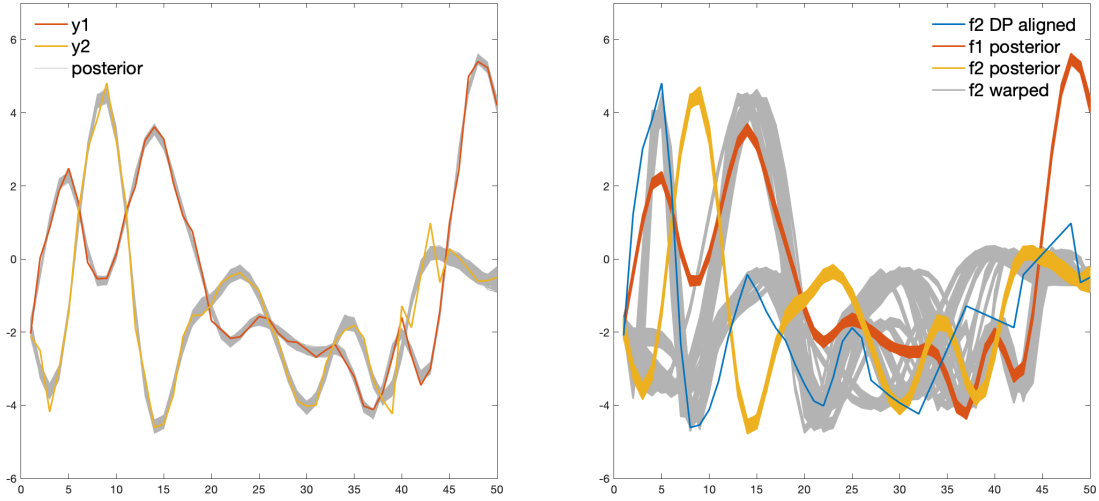


Figure 7: Posteriors $f_1|y_1$ and $f_2|y_2$ shown in gray compared to the raw data y_1 and y_2 (left). The posterior of the warped function $(f_2 \circ \gamma)|y_1, y_2$ captures a more accurate alignment than the single DP warped solution in blue (right).

Figure 8 on the left compares the DP solution to the posterior distribution of $\gamma|y_1, y_2$ and shows the posterior median and 95% credible region of $\gamma|y_1, y_2$. The credible region quantifies the uncertainty around the estimated warping function γ and warped function $(f_2 \circ \gamma)$. The DP solution, obtained by trying to align the noisy data without prior data smoothing, is not built to account for the multiple possible alignments.

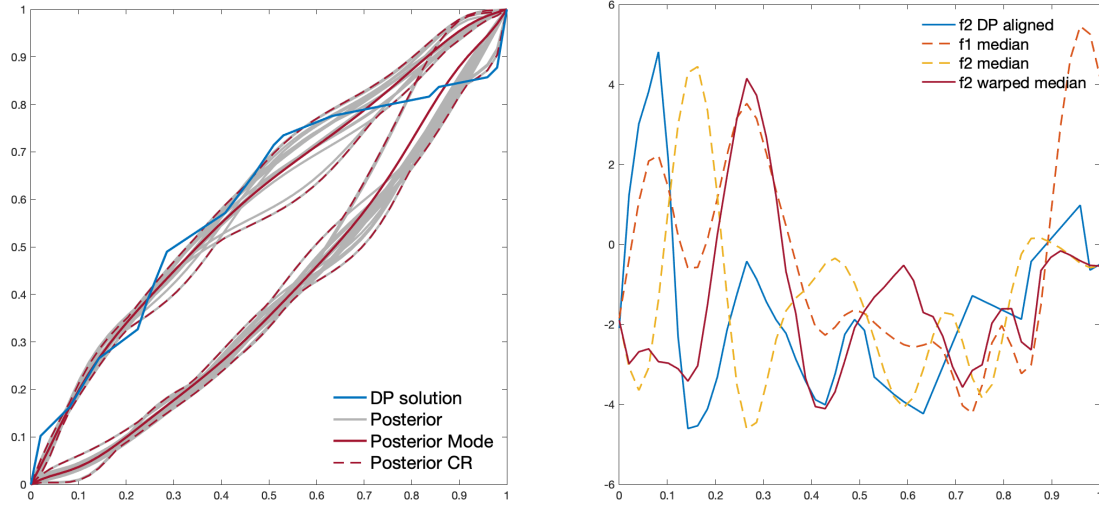


Figure 8: Comparison of the posterior distribution $\gamma|y_1, y_2$ to the DP solution γ_{DP} applied to the iPhone data, plotting the two identified modes and respective 95% credible regions of the posterior $\gamma|y_1, y_2$ (left). Comparison of the DP warping of y_2 to the median of the warping $f_2 \circ \gamma|y_1, y_2$ (right).

5. Discussion

We have proposed a new flexible Bayesian approach to functional alignment that handles measurement error and accounts for multiple optimal alignments in the posterior of the warping function γ . We have demonstrated its advantages over the state-of-the-art Dynamic Programming method that has been used in recent alignment literature [Srivastava and Klassen \(2016\)](#); [Srivastava et al. \(2011a\)](#); [Tucker et al. \(2013\)](#) using both simulated and real datasets. Unlike DP, a Bayesian approach can characterize the uncertainty in the warping function solution γ with Bayesian credible intervals. The hierarchical structure of our Bayesian method allows us to estimate measurement error observed in y_1 and y_2 and extract the mean functions f_1 and f_2 to be aligned, respectively.

Accounting for measurement error directly in the method itself avoids any need for smoothing of the data typically done prior to applying DP in practice. Additionally, by running parallel MCMC chains, the posterior of the warping function γ is able to capture all possible alignments and visualize the posterior modes and respective credible regions for one or more distinct alignments. Although existing Bayesian methods can account for uncertainty in the warping function, they are not able to find more than one possible alignment because they focus on converging efficiently to one solution and do not account for measurement uncertainty. Without accounting for all possible alignments, we are missing information and not accounting for all uncertainty in γ .

For future work we look to extend the method to the multiple alignment problem. This will not be trivial in the case of multi-modal posteriors and multi-function alignment as the solution will not be as simple as running multiple chains, and the use of wormhole MCMC ([Lan et al. \(2014\)](#)) or something similar would need to be explored. Additionally, we can extend this from curves to trajectories that lie on Riemannian manifolds \mathcal{M} . In this case, one has to account for the non-zero curvature of the space and in particular, the calculation of the gradient in the Fisher Rao metric.

Acknowledgment

This paper describes objective technical results and analysis. Any subjective views or opinions that might be expressed in the paper do not necessarily represent the views of the U.S. Department of Energy or the United States Government. This work was supported by the Laboratory Directed Research and Development program at Sandia National Laboratories, a multi-mission laboratory managed and operated by National Technology and Engineering Solutions of Sandia, LLC, a wholly owned subsidiary of Honeywell International, Inc., for the U.S. Department of Energy’s National Nuclear Security Administration under contract DE-NA0003525.

References

- Beskos, A., Girolami, M., Lan, S., Farrell, P.E., 2017. Geometric mcmc for infinite-dimensional inverse problems. *Journal of Computational Physics* 335, 327–351.
- Beskos, A., Pinski, F.J., Sanz-Serna, J.M., Stuart, A.M., 2011. Hybrid monte carlo on hilbert spaces. *Stochastic Processes and their Applications* 121, 2201–2230.
- Bhattachayya, A., 1943. On a measure of divergence between two statistical populations defined by their population distributions. *Bulletin Calcutta Mathematical Society* 35, 99–109.
- Cheng, W., Dryden, I.L., Huang, X., 2016. Bayesian registration of functions and curves. *Bayesian Analysis* 11, 447–475.
- Cotter, S.L., Roberts, G.O., Stuart, A.M., White, D., 2013. Mcmc methods for functions: modifying old algorithms to make them faster. *Statistical Science* 28, 424–446.
- Hesthaven, J.S., Gottlieb, S., Gottlieb, D., 2007. *Spectral Methods for Time-Dependent Problems*. Cambridge Monographs on Applied and Computational Mathematics, Cambridge University Press.
- Kargl, S., Williams, K., Marston, T., Kennedy, J., Lopes, J., 2010. Acoustic response of unexploded ordnance (UXO) and cylindrical targets. *Proc. of MTS/IEEE Oceans 2010 Conference*, 1–5.
- Kneip, A., Ramsay, J.O., 2008. Combining registration and fitting for functional models. *Journal of the American Statistical Association* 103.
- Kurtek, S., 2017. A geometric approach to pairwise bayesian alignment of functional data using importance sampling. *Electronic Journal of Statistics* 11, 502–531.
- Kurtek, S., Srivastava, A., Klassen, E., Ding, Z., 2012. Statistical modeling of curves using shapes and related features. *Journal of the American Statistical Association* 107, 1152–1165.
- Lan, S., Streets, J., Shahbaba, B., 2014. Wormhole hamiltonian monte carlo. *Proc Conf AAAI Artif Intell* 33, 1953–1959.
- Lu, Y., Herbei, R., Kurtek, S., 2017. Bayesian registration of functions with a gaussian process prior. *Journal of Computational and Graphical Statistics* 26, 894–904.
- Marron, J., Ramsay, J., Sangalli, L., Srivastava, A., 2015. Functional data analysis of amplitude and phase variation. *Statistical Science* 30, 468–484.
- Matuk, J., Bharath, K., Chkrebtii, O., Kurtek, S., 2019. Bayesian framework for simultaneous registration and estimation of noisy, sparse and fragmented functional data. *arXiv:1912.05125 [stat.ME]* URL: <https://arxiv.org/abs/1912.05125>.
- McCall, C., Reddy, K., Shah, M., 2012. Macro-class selection for hierarchical K-NN classification of inertial sensor data. *Proc. of PECCS 2012*.
- Nishimura, A., Dunson, D., 2017. Geometrically tempered hamiltonian monte carlo.
- Ramsay, J.O., Silverman, B.W., 2005. *Functional Data Analysis*. Springer.
- Sangalli, L.M., Secchi, P., Vantini, S., Vitelli, V., 2010. Functional clustering and alignment methods with applications. *Communications in Applied and Industrial Mathematics* 1, 205–224.
- Srivastava, A., Jermyn, I., Joshi, S., 2007. Riemannian analysis of probability density functions with applications in vision, in: *IEEE Conference on Computer Vision and Pattern Recognition*, pp. 1–8.
- Srivastava, A., Klassen, E., Joshi, S., Jermyn, I., 2011a. Shape analysis of elastic curves in euclidean spaces. *IEEE Transactions on Pattern Analysis and Machine Intelligence* 33, 1415–1428.
- Srivastava, A., Klassen, E.P., 2016. *Functional and Shape Data Analysis*. Springer-Verlag.
- Srivastava, A., Wu, W., Kurtek, S., Klassen, E., Marron, J.S., 2011b. Registration of functional data using Fisher-Rao metric. *arXiv:1103.3817v2 [math.ST]* URL: <http://arxiv.org/abs/1103.3817v2>.

- Telesca, D., Inoue, L.Y.T., 2008. Bayesian hierarchical curve registration. *Journal of the American Statistical Associations* 103, 328–339.
- Tucker, J.D., Wu, W., Srivastava, A., 2013. Generative models for functional data using phase and amplitude separation. *Computational Statistics and Data Analysis* 61, 50–66.
- Xie, W., Kurtek, S., Bharath, K., Sun, Y., 2017. A geometric approach to visualization of variability in functional data. *Journal of American Statistical Association* 112, 979–993.

Appendix A. Derivative of $\Phi(g)$

In this section we provide the derivations to compute the derivative of the negative log-likelihood, $\nabla\Phi(\psi) = \frac{d\Phi}{d\psi}$. The negative log-likelihood is defined

$$\Phi := -\log L(\psi, \sigma_1^2) = \frac{N}{2} \log(\sigma_1^2) + \frac{1}{2\sigma_1^2} \int_0^1 \left(q_1(t) - (q_2(\int_0^t \psi^2(s) ds) \psi(t)) \right)^2 dt.$$

To compute the directional derivative, let $A(t) = q_1(t) - (q_2(\int_0^t \psi^2(s) ds) \psi(t))$ and we will rewrite $\nabla\Phi(\psi)$ for simplicity as

$$\nabla\Phi(\psi) = \frac{1}{\sigma_1^2} \int_0^1 A(t) \nabla_\psi A(t) dt.$$

To find the directional derivative $\nabla_\psi A(t_i)$, we first, consider the sequence of maps $\psi \xrightarrow{\int_0^t \psi^2 ds} \gamma \xrightarrow{\phi} r$, where $r := \phi(\gamma) = (q \circ \gamma) \sqrt{\gamma}$. For the constant function $\mathbf{1} \in \Psi$ and a tangent vector $u \in T_{\mathbf{1}}(\mathbb{S}_\infty)$ the differential of the first mapping at $\mathbf{1}$ is $2\bar{u}(t) = 2 \int_0^t u(s) ds$. For a tangent vector $w \in T_{\gamma_{id}}(\Gamma)$, the differential of the second mapping at $\gamma_{id} = t$ is $\frac{\partial \tilde{q}}{\partial t} w + \frac{1}{2} \tilde{q} \dot{w}$, where $\tilde{q} = q(\int_0^t \psi(s)^2 ds) \psi$. If we concatenate these two linear maps we obtain the directional partial derivative of $A(\psi)$ in a direction $u \in T_{\mathbf{1}}(\mathbb{S}_\infty)$ as

$$\nabla_\psi A(u) = -2 \frac{\partial \tilde{q}_2}{\partial t} \bar{u}(t) - \tilde{q}_2 u(t).$$

We now can write the derivative of Φ in the direction of u as

$$\nabla_\psi \Phi(u) = \frac{1}{\sigma_1^2} \int_0^1 A(t) \nabla_\psi A(u) dt.$$

Since $T_{\mathbf{1}}(\mathbb{S}_\infty)$ is an infinite-dimensional space, we can approximate the directional partial derivative by considering a finite-dimensional subspace of $T_{\mathbf{1}}(\mathbb{S}_\infty)$. Let us form a subspace of $T_{\mathbf{1}}(\mathbb{S}_\infty)$ using $\{(\frac{1}{\sqrt{\pi}} \sin(2\pi nt), \frac{1}{\sqrt{\pi}} \cos(2\pi nt)) \mid n = 1, 2, \dots, p/2\}$. We then can approximate the derivative using

$$\nabla_\psi \Phi = \sum_{i=1}^p \nabla_\psi \Phi(c_i) c_i,$$

where c_i 's are the basis elements of the subspace.

Appendix B. MCMC diagnostics

In this section, we show select MCMC diagnostic plots for the three examples demonstrated in this paper. We show the accepted samples for σ_1^2 and σ_2^2 for all chains run in parallel which show the good mixing and convergence of $f_1|y_1$ and $f_2|y_2$. We also show the accepted samples for σ^2 for

each chain separately to show convergence of $(q_1 - \mathcal{G}(g(t)))|y_1, y_2$ for each chain. Lastly, we show the accepted samples for the n_v basis coefficients B for all chains to show their ability to jump between modes and mix well within a mode. Note that due to the high efficiency of the ∞ -HMC algorithm and necessary burn-in to ensure all parameters converge, we expect the relatively low acceptance rates for $(g, \theta)|y_1, y_2$ observed in the right hand figure of Figures B.9, B.10, and B.11 below.

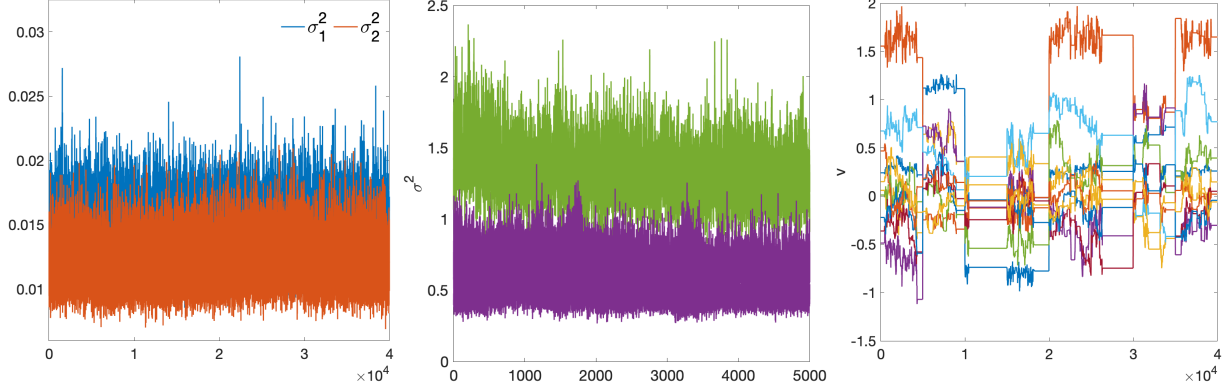


Figure B.9: From left to right: MCMC chains from the simulated data results shown in Section 4.1 for σ_1^2 (blue), σ_2^2 (orange), σ^2 for all 8 chains separately colored by the posterior cluster they are associated with, and v for all chains).

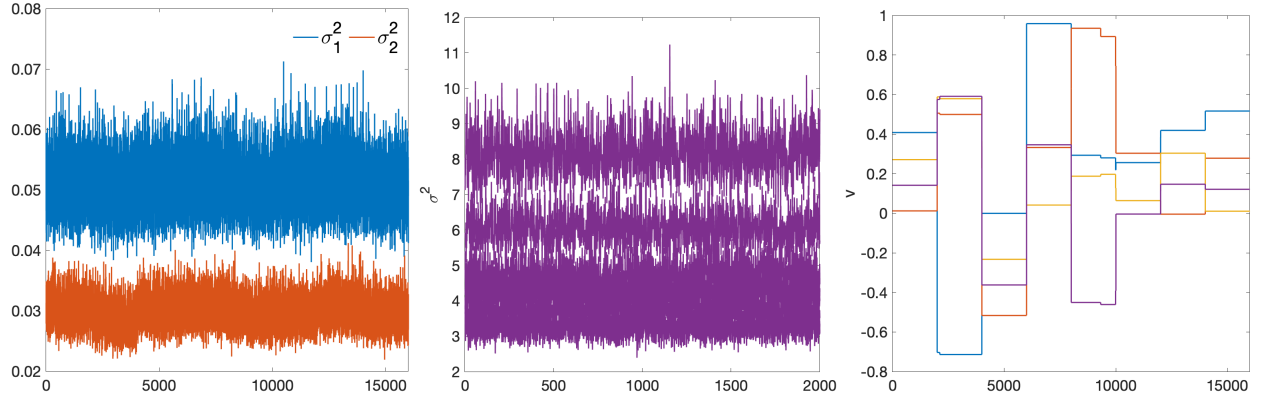


Figure B.10: From left to right: MCMC chains from the SONAR data results shown in Section 4.3 for σ_1^2 (blue), σ_2^2 (orange), σ^2 for all 8 chains separately (middle) colored by the posterior cluster they are associated with, and v for all chains).

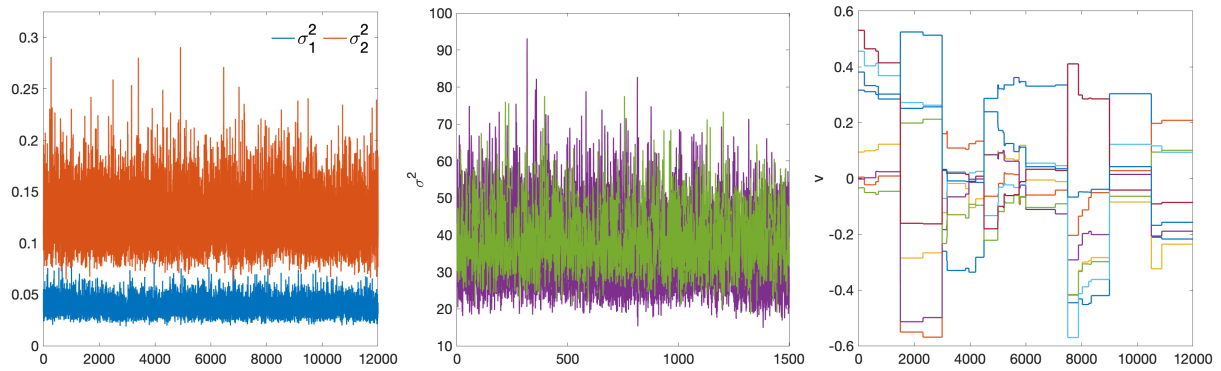


Figure B.11: From left to right: MCMC chains from the iPhone data results shown in Section 4.3 for σ_1^2 (blue), σ_2^2 (orange), σ^2 for all 8 chains separately colored by the posterior cluster they are associated with, and \mathbf{v} for all chains.